

# A LiDAR-Aided Channel Model for Vehicular Intelligent Sensing-Communication Integration

Ziwei Huang, *Graduate Student Member, IEEE*, Lu Bai, *Member, IEEE*,  
Mingran Sun, *Graduate Student Member, IEEE*, and Xiang Cheng, *Fellow, IEEE*

**Abstract**—In this paper, a novel channel modeling approach, named light detection and ranging (LiDAR)-aided geometry-based stochastic modeling (LA-GBSM), is developed. Based on the developed LA-GBSM approach, a new millimeter wave (mmWave) channel model for sixth-generation (6G) vehicular intelligent sensing-communication integration is proposed, which can support the design of intelligent transportation systems (ITSs). The proposed LA-GBSM is accurately parameterized under high, medium, and low vehicular traffic density (VTD) conditions via a sensing-communication simulation dataset with LiDAR point clouds and scatterer information for the first time. Specifically, by detecting dynamic vehicles and static building/tress through LiDAR point clouds via machine learning, scatterers are divided into static and dynamic scatterers. Furthermore, statistical distributions of parameters, e.g., distance, angle, number, and power, related to static and dynamic scatterers are quantified under high, medium, and low VTD conditions. To mimic channel non-stationarity and consistency, based on the quantified statistical distributions, a new visibility region (VR)-based algorithm in consideration of newly generated static/dynamic scatterers is developed. Key channel statistics are derived and simulated. By comparing simulation results and ray-tracing (RT)-based results, the utility of the proposed LA-GBSM is verified.

**Index Terms**—6G, vehicular intelligent sensing-communication integration, simulation dataset, LiDAR-aided channel model.

## I. INTRODUCTION

IN the upcoming sixth-generation (6G) era, the vehicular communication network, which is a key component in the intelligent transportation system (ITS), is expected to support more potential applications associated with future vehicles, including autonomous and smart vehicles. Bearing safety and efficiency as the utmost aims, autonomous and smart vehicles are equipped with multi-modal sensors. These sensors are wirelessly connected to provide comprehensive environmental feature for the transportation purpose [1]. Therefore, the integration of multi-modal sensing and communications is henceforth pivotal and natural in the vehicular communication network [2]. However, it cannot be adequately supported by the extensively studied integrated sensing and communications (ISAC), which limits to the integration of radio-frequency

(RF) based radar sensing and communications. To fill this gap, inspired by human synesthesia, i.e., an involuntary human neuropsychological trait in which the stimulation of one human sense evokes another human sense, [3] proposes a novel concept, i.e., *Synesthesia of Machines (SoM)*. SoM refers to intelligent multi-modal sensing-communication integration. Similar to how human senses the surrounding environment via multiple organs, multi-modal sensors and communication devices can also obtain environmental information, and thus we analogously refer to them as “machine senses” in SoM. Furthermore, the environmental information obtained by multiple organs can be mutually facilitated via complex biological neural networks in human synesthesia. Similarly, in SoM, the environmental information obtained by “machine senses” can be processed via machine learning in an intelligent manner to achieve mutual facilitation. Unlike ISAC, which solely includes the integration of sensing and communications in RF, SoM refers to the intelligent integration of multi-modal sensing and communications, including RF communications, RF sensing, i.e., millimeter wave (mmWave) radar, and non-RF sensing, i.e., light detection and ranging (LiDAR) and RGB-D cameras etc. Therefore, SoM is a more generalized concept than ISAC and ISAC can be regarded as a special case of SoM. As a typical application scenario in SoM, vehicular intelligent sensing-communication integration in ITSs has been received extensive attention. To support the design of vehicular intelligent sensing-communication integration systems, the proper characterization and modeling of underlying channels are essential [3], [4].

Currently, the characterization and modeling of vehicular channels and the revealing of channel characteristics are based on vehicular channel measurement campaigns [5]. The authors in [6] carried out vehicle-to-vehicle (V2V) channel measurement campaigns at 5.2 GHz in highway and rural scenarios in Lund, Sweden. In [6], time non-stationarity of rapidly-changing V2V channels was revealed, whereas the appearance and disappearance of scatterers were disregarded. The authors in [7] conducted a different V2V channel measurement campaign at 5.9 GHz in viaduct, tunnel, and cutting scenarios, where time non-stationarity of V2V channels and smooth scatterer evolution in the time domain were explored. However, the existing V2V channel measurement campaigns, e.g., [6] and [7], solely processed the RF channel information collected by communication devices, without the facilitation of the sensory information collected by sensors. The lack of sensory information results in the fact that the transceiver cannot detect dynamic objects and static objects. In this case,

The authors would like to thank Boxun Liu and Yong Yu for their help in the collection of LiDAR point clouds in AirSim simulation platform.

Z. Huang, M. Sun, and X. Cheng are with the State Key Laboratory of Advanced Optical Communication Systems and Networks, School of Electronics, Peking University, Beijing, 100871, P. R. China (email: ziwei-huang@pku.edu.cn, mingransun@stu.pku.edu.cn, xiangcheng@pku.edu.cn).

L. Bai is with the Joint SDU-NTU Centre for Artificial Intelligence Research (C-FAIR), Shandong University, Jinan, 250101, P. R. China (e-mail: lubai@sdu.edu.cn).

it is significantly difficult to distinguish dynamic scatterers and static scatterers, which are certain objects, e.g., dynamic vehicles or static buildings/trees, in the physical environment [8]–[10]. Due to the inability to distinguish dynamic and static scatterers, the vehicular channel characteristics under different vehicular traffic density (VTD) conditions cannot be explored. However, to support 6G applications for vehicular intelligent sensing-communication integration in ITSs, such as target localization and tracking for autonomous vehicles, it is necessary to conduct precise environment modeling and explore vehicular channel characteristics under different VTD conditions [2]. Therefore, the existing vehicular channel measurement campaigns that solely process RF channel information cannot adequately reveal channel characteristics.

Based on the vehicular channel characteristics revealed by channel measurement campaigns, extensive vehicular channel models have been proposed. To model time non-stationarity, the authors in [11] and [12] utilized the methods of capturing time-varying channel statistics and birth-death process, respectively. However, the proposed models in [11], [12] cannot explore the impact of VTDs on vehicular channel characteristics. To overcome this limitation, the authors in [13] proposed a V2V channel model and attempted to explore the vehicular channel characteristics under high and low VTD conditions by dividing static and dynamic scatterers. To further model time non-stationarity in consideration of VTDs, the authors in [14] proposed a V2V channel model and used the birth-death process to characterize the appearances and disappearances of static scatterers and dynamic scatterers, respectively. When the mmWave technology is used to high-mobility vehicular communications, it is pivotal to further capture time consistency and time-frequency non-stationarity [4]. Towards this objective, our previous work in [15] used VTD-based visibility region (VR) and modeled frequency-dependent path gain for the components via static scatterers and dynamic scatterers. However, the existing vehicular channel models in [13]–[15] are solely at the stage of simply distinguishing static scatterers and dynamic scatterers for the modeling of VTDs. On the one hand, to model different VTD conditions, the existing vehicular channel models simply adjusted the numbers of dynamic and static scatterers, while ignored other key parameters, such as distance, angle, and delay-power. According to the standardized channel models, e.g., [16], [17], the simultaneous investigation of number, distance, angle, and delay-power parameters is important. On the other hand, since the determination of VR in different VTD conditions is not based on high-fidelity data, the smooth evolution of dynamic and static scatterers cannot be realistically characterized. Therefore, the existing vehicular channel models that mimic different VTD conditions by simply distinguishing dynamic and static scatterers cannot support the vehicular sensing and communication system design and autonomous driving. Specifically, various non-RF sensors, e.g., LiDAR, onboard autonomous vehicles can detect dynamic and static objects [18], and further align with the channel information collected by communication devices to distinguish dynamic and static scatterers under different VTD conditions. In such a condition, it is urgent to have a precise and comprehensive

modeling of the parameters and smooth evolution of dynamic and static scatterers.

To fill this gap, we conduct a comprehensive channel characterization and modeling for vehicular intelligent sensing-communication integration based on a sensing-communication dataset. Thanks to the intelligent integration of sensing and communications, sensory data can be combined with communication data to support channel characterization and modeling [1]. Towards this objective, a comprehensive sensing-communication dataset, which contains sensory data and communication data, is essential. According to the dataset acquisition way, the existing datasets can be divided into measurement datasets and simulation datasets. Measurement datasets are directly collected by the measurement equipment. Despite the measurement dataset, e.g., [19], can support the verification of fundamental methods, it is hard to flexibly customize the desired scenario because of the labor and cost concerns. Unlike measurement datasets, the simulation dataset achieves a decent trade-off between complexity and fidelity via efficient software, and thus receives extensive attention. Nonetheless, there is no software that can simultaneously collect sensory data and communication data. With the LiDAR simulator in [20] and Wireless InSite [21], a sensing-communication simulation dataset, named LiDAR-COM in this paper, was constructed in [22]. In [23], a different sensing-communication simulation dataset, named Vision-Wireless (ViWi), was proposed based on Wireless InSite and a popular game engine, i.e., Blender<sup>TM</sup>. However, the rendering of scenarios in the LiDAR-COM dataset [22] and the ViWi dataset [23] was relatively rough and the V2V channel data was ignored. To overcome these limitations, we constructed a sensing-communication simulation dataset in [24] with superior rendering effects and V2V channel data. The sensing-communication dataset in [24] contains high-fidelity sensory data collected by AirSim [25] and communication data collected by Wireless InSite [21]. With the help of the sensing-communication simulation dataset in [24], inspired by the potential facilitation of sensory information on communications in SoM [3], a novel channel modeling approach, named LiDAR-aided geometry-based stochastic modeling (LA-GBSM), is developed. The developed LA-GBSM approach utilizes LiDAR point clouds to facilitate the revelation of channel characteristics, and further leverages geometry-based stochastic modeling (GBSM) to model channels based on the revealed channel characteristics. By using the developed LA-GBSM approach, a novel non-stationary and consistent mmWave channel model for vehicular intelligent sensing-communication integration is proposed. Although the proposed LA-GBSM utilizes single-modal sensory data, it for the first time exploits non-RF sensory data, which is processed by machine learning in an intelligent manner, to facilitate RF channel modeling. Currently, the existing channel measurements and models solely process channel information and ignore the facilitation of sensory information, and thus cannot support SoM research. The main contributions and novelties of this paper are summarized below.

- 1) With the help of LiDAR point clouds that are intelligently processed by machine learning, a novel chan-

nel modeling approach, i.e., LA-GBSM, is developed. Based on the LA-GBSM approach, a new non-stationary and consistent mmWave channel model is proposed for vehicular intelligent sensing-communication integration under high, medium, and low VTD conditions. The proposed LA-GBSM is adequately parameterized by the high-fidelity sensing-communication dataset in [24].

- 2) In the proposed LA-GBSM, the number, distance, angle, and power-delay statistical distributions of dynamic and static scatterers under high, medium, and low VTD conditions are obtained via LiDAR point clouds for the first time. This fills the gap that the existing channel measurement campaign without the facilitation of sensory information cannot obtain these statistical distributions as it is exceedingly difficult to divide dynamic and static scatterers solely by Doppler information in RF channels.
- 3) To capture time non-stationarity and consistency, based on the obtained statistical distributions tailored for high, medium, and low VTD conditions, a new VR-based algorithm in consideration of newly generated static/dynamic clusters is developed to mimic smooth cluster evolution. Furthermore, a frequency-dependent factor is introduced to model frequency non-stationarity.
- 4) Key channel statistical properties, including time-frequency correlation function (TF-CF) and Doppler power spectral density (DPSD), are derived and simulated. The close agreement between simulation results and ray-tracing (RT)-based results is achieved to verify the proposed LA-GBSM.

The remainder of this paper is organized as follows. Section II describes the scenario of the sensing-communication simulation dataset and the intelligent processing of data. Section III presents channel characterization under high, medium, and low VTD conditions. In Section IV, a novel non-stationary and consistent LA-GBSM for vehicular intelligent sensing-communication integration is proposed. Key channel statistical properties are given in Section V. Section VI presents the simulation result, which is further compared with the RT-based result. Finally, Section VII draws the conclusions.

## II. SIMULATION TESTING FOR VEHICULAR INTELLIGENT SENSING-COMMUNICATION INTEGRATION

Based on the sensing-communication simulation dataset in [24], LiDAR point clouds and channel data are intelligently processed to determine static and dynamic scatterers.

### A. Simulation Dataset in Vehicular Urban Crossroad with Different VTD Conditions

In [24], a high-fidelity sensing-communication simulation dataset was constructed based on two accurate simulation platforms, i.e., Wireless InSite [21] and AirSim [25]. Wireless InSite [21] uses RT technology based on geometrical optics and the uniform theory of diffraction to obtain accurate channel data. AirSim [25] constructs the simulation scenario by using advanced three-dimensional (3D) modeling software with superior rendering effects, and thus can collect precise

TABLE I  
NUMBERS OF LIDAR POINT CLOUDS AND LINKS WITH SCATTERERS UNDER HIGH, MEDIUM, AND LOW VTD CONDITIONS.

Condition	LiDAR point clouds	Links with scatterers
High VTD	3,600	43,200
Medium VTD	3,000	30,000
Low VTD	1,800	10,800
<b>Total</b>	<b>8,400</b>	<b>84,000</b>

sensory data. Here, a typical urban crossroad scenario of vehicular intelligent sensing-communication integration in [24] with high, medium, and low VTD conditions is considered. The numbers of vehicles in high, medium, and low VTD conditions are 20, 12, and 8, respectively. Fig. 1 depicts the scenarios with high, medium, and low VTD conditions at the initial snapshot. The number of snapshots in each VTD condition is 300. Each car/bus is mobile and is equipped with the LiDAR device and communication equipment. The sensory data is collected by the LiDAR device, which has 16 channels, 10 Hz scanning frequency, 240,000 points per second,  $-20^\circ \sim 20^\circ$  horizontal field of view (FoV), and  $-25^\circ \sim 0^\circ$  vertical FoV. The communication data is obtained at a typical mmWave frequency band, i.e.,  $f_c = 28$  GHz carrier frequency with 2 GHz communication bandwidth. The numbers of antennas at transmitter (Tx) and receiver (Rx) are  $M_T = M_R = 1$ . In each communication link, e.g., Car1 is the Tx and Car2 is the Rx, the 3D coordinates of scatterers are obtained. For clarity, Table I gives the numbers of the obtained sensory and communication data.

### B. Intelligent Processing of Simulation Dataset

In this subsection, steps of distinguishing dynamic scatterers and static scatterers are given.

The first step is to align electromagnetic environment with physical environment through coordinate transformation of LiDAR point clouds. The coordinate of sensor is given as  $\mathbf{S}(t) = [x_{\text{sen}}(t), y_{\text{sen}}(t), z_{\text{sen}}(t)]$  and the relative coordinate of the LiDAR point cloud is given as  $\mathbf{L}'(t) = [x_{\text{Li}}(t), y_{\text{Li}}(t), z_{\text{Li}}(t)]$ . When the sensor moves in the positive  $x$ -axis, negative  $x$ -axis, positive  $y$ -axis, and negative  $y$ -axis directions, the absolute coordinates of the point cloud are respectively expressed as

$$\mathbf{L}_x^p(t) = [x_{\text{Li}}(t) + x_{\text{sen}}(t), -y_{\text{Li}}(t) - y_{\text{sen}}(t), -z_{\text{Li}}(t) - z_{\text{sen}}(t)] \quad (1)$$

$$\mathbf{L}_x^n(t) = [-x_{\text{Li}}(t) + x_{\text{sen}}(t), y_{\text{Li}}(t) + y_{\text{sen}}(t), -z_{\text{Li}}(t) - z_{\text{sen}}(t)] \quad (2)$$

$$\mathbf{L}_y^p(t) = [y_{\text{Li}}(t) + x_{\text{sen}}(t), x_{\text{Li}}(t) + y_{\text{sen}}(t), -z_{\text{Li}}(t) - z_{\text{sen}}(t)] \quad (3)$$

$$\mathbf{L}_y^n(t) = [-y_{\text{Li}}(t) + x_{\text{sen}}(t), -x_{\text{Li}}(t) + y_{\text{sen}}(t), -z_{\text{Li}}(t) - z_{\text{sen}}(t)] \quad (4)$$

Fig. 2(a) depicts LiDAR point clouds and scatterers under medium VTDs at initial time, where Car3 is the Rx and Car1 is equipped with the LiDAR device and is also the Tx. It can be seen from Fig. 2(a) that scatterers are generally located on LiDAR point clouds, and thus the alignment between electromagnetic environment and physical environment is achieved.

The second step is the object classification based on the coordinates of LiDAR point clouds. However, extensive LiDAR points are ground points, which appear as a texture and

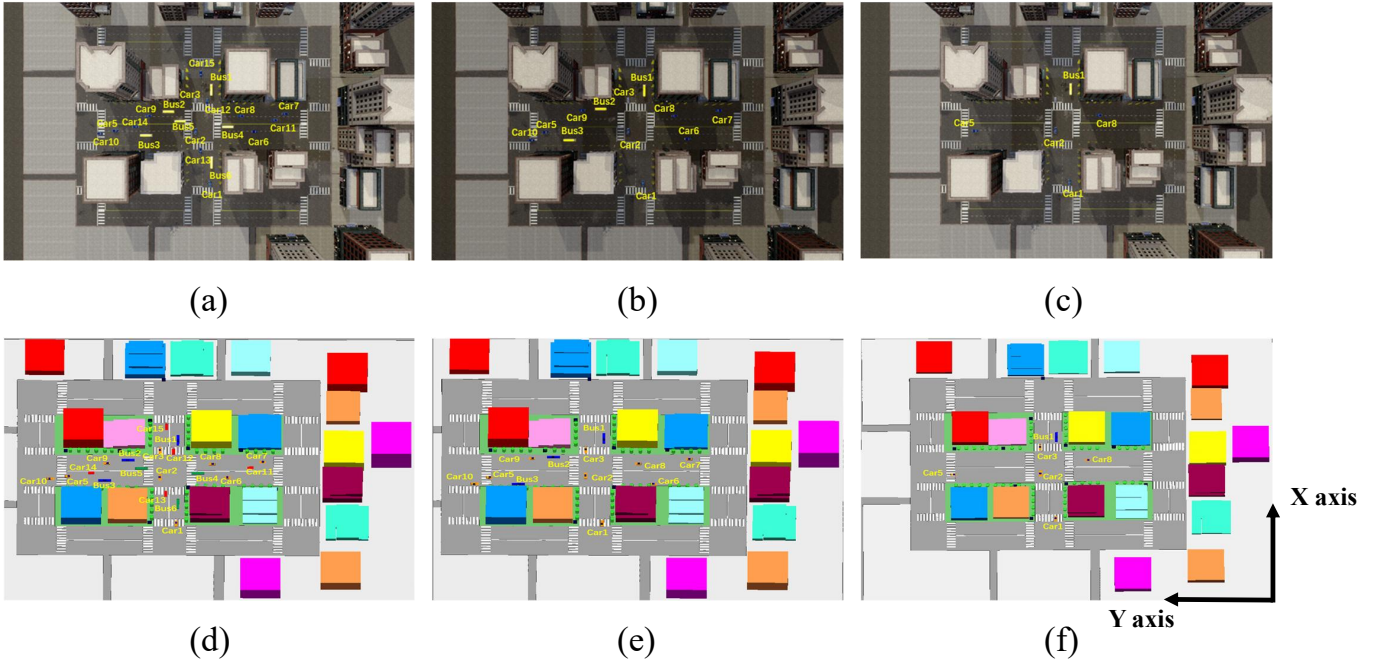


Fig. 1. Vehicular simulation scenarios at the initial snapshot. Figs. (a)–(c) are the scenarios in AirSim under high, medium, and low VTDs, respectively. Figs. (d)–(f) are the scenarios in Wireless InSite under high, medium, and low VTDs, respectively.

significantly interfere with object point cloud processing. To reduce the amount of data and improve the accuracy of the object classification, the ground point needs to be removed via the pre-processing of LiDAR point clouds. Then, LiDAR point clouds solely include the information related to static objects and dynamic vehicles in the environment.

The third step is to distinguish between dynamic vehicles and static objects based on LiDAR point clouds. A typical *machine learning algorithm*, i.e., DBSCAN clustering, is exploited. According to the clustering result, the maximum and minimum values of the  $x/y/z$ -axis coordinates in a cluster are calculated. Since the size of vehicle is small, it is detected as a dynamic vehicle if the difference between the maximum and minimum values of the  $x$ ,  $y$ , and  $z$ -axis coordinates for a cluster is less than the size threshold on the  $x$ ,  $y$ , and  $z$ -axis, respectively. Otherwise, the cluster is detected as a static object, such as roadside trees and buildings.

The fourth step is to determine static scatterers and dynamic scatterers in electromagnetic environment. Based on the detected dynamic/static objects and aligned electromagnetic and physical environments, we classify scatterers as dynamic scatterers, static scatterers, and unknown scatterers. If the scatterer coincides with the detected dynamic/static object, it is a dynamic/static scatterer. The remaining scatterers are named unknown scatterers, which do not coincide with LiDAR points. The physical mechanism underlying the appearance of unknown scatterers is that they are beyond the detection range of the LiDAR device. In general, the unknown scatterer is far away from the transceiver, and thus can be ignored in channel realization due to the high path loss under mmWave communications. Fig. 2(b) shows LiDAR point clouds and scatterers after DBSCAN clustering from the bird's eye view (BEV) perspective, where Car3 is the Rx and Car1 is the Tx

and is also equipped with the LiDAR device. In Fig. 2(b), vehicles are precisely detected and there are static, dynamic, and unknown scatterers. Therefore, in the fourth step, the 3D coordinates of static and dynamic scatterers can be obtained.

### III. VEHICULAR INTELLIGENT SENSING-COMMUNICATION INTEGRATION CHANNEL CHARACTERIZATION

Currently, it is exceedingly difficult to distinguish static and dynamic scatterers via channel measurement campaigns as they solely process Doppler information in RF channels, i.e., without the facilitation of sensory information. In such a case, there is no vehicular channel measurement campaign that can adequately characterize channels for vehicular intelligent sensing-communication integration under different VTD conditions. Nevertheless, the accurate modeling of VTDs is of paramount importance for the proper channel characterization [26]. To fill this gap, by intelligently processing LiDAR point clouds and channel information, the statistical distributions of parameters related to static and dynamic scatterers are explored under different VTD conditions. The statistical values are summarized in Table II. Consequently, we tailor static/dynamic scatterer parameters for the modeling of vehicular intelligent sensing-communication integration channels under different VTD conditions.

#### A. Scatterer and Cluster Numbers

In channel realization, the proper modeling of scatterer and cluster numbers is important [27], [28]. However, in [29], the number of scatterers was modeled to obey the linear distribution and the distinction between dynamic scatterers and static scatterers was ignored. Meanwhile, the authors in

TABLE II  
KEY STATISTICAL PARAMETERS IN V2V SENSING AND COMMUNICATION INTEGRATION CHANNELS

Parameter	Distribution	Type	VTD	Value	
Number	Logistic	Static cluster	High	$\mu_s^{c,L} = 0.09, \gamma_s^{c,L} = 0.03$	
			Medium	$\mu_s^{c,L} = 0.14, \gamma_s^{c,L} = 0.04$	
			Low	$\mu_s^{c,L} = 0.08, \gamma_s^{c,L} = 0.03$	
		Dynamic cluster	High	$\mu_d^{c,L} = 0.12, \gamma_d^{c,L} = 0.06$	
			Medium	$\mu_d^{c,L} = 0.09, \gamma_d^{c,L} = 0.03$	
			Low	$\mu_d^{c,L} = 0.06, \gamma_d^{c,L} = 0.03$	
		Static scatterer	High	$\mu_s^{s,L} = 0.45, \gamma_s^{s,L} = 0.15$	
			Medium	$\mu_s^{s,L} = 0.82, \gamma_s^{s,L} = 0.23$	
			Low	$\mu_s^{s,L} = 0.49, \gamma_s^{s,L} = 0.16$	
		Dynamic scatterer	High	$\mu_d^{s,L} = 0.53, \gamma_d^{s,L} = 0.25$	
			Medium	$\mu_d^{s,L} = 0.44, \gamma_d^{s,L} = 0.18$	
			Low	$\mu_d^{s,L} = 0.28, \gamma_d^{s,L} = 0.17$	
Distance	Gamma	Static scatterer	High	$\alpha_s^G = 0.68, \beta_s^G = 1.74$	
			Medium	$\alpha_s^G = 0.83, \beta_s^G = 1.71$	
			Low	$\alpha_s^G = 0.59, \beta_s^G = 2.08$	
	Rayleigh	Dynamic scatterer	High	$\sigma_d^R = 0.55$	
			Medium	$\sigma_d^R = 0.37$	
			Low	$\sigma_d^R = 0.30$	
Angle	AAoD	Gaussian	Static scatterer	High	$\mu_s^{AAoD} = -0.48, \sigma_s^{AAoD} = 1.85$
				Medium	$\mu_s^{AAoD} = -0.12, \sigma_s^{AAoD} = 2.08$
				Low	$\mu_s^{AAoD} = 0.26, \sigma_s^{AAoD} = 1.76$
		Dynamic scatterer	High	$\mu_d^{AAoD} = -0.72, \sigma_d^{AAoD} = 1.98$	
			Medium	$\mu_d^{AAoD} = -0.54, \sigma_d^{AAoD} = 1.78$	
			Low	$\mu_d^{AAoD} = -0.09, \sigma_d^{AAoD} = 1.73$	
	AAoA	Gaussian	Static scatterer	High	$\mu_s^{AAoA} = 0.28, \sigma_s^{AAoA} = 1.89$
				Medium	$\mu_s^{AAoA} = 0.52, \sigma_s^{AAoA} = 1.95$
				Low	$\mu_s^{AAoA} = 0.35, \sigma_s^{AAoA} = 1.71$
		Dynamic scatterer	High	$\mu_d^{AAoA} = 0.62, \sigma_d^{AAoA} = 1.98$	
			Medium	$\mu_d^{AAoA} = 0.81, \sigma_d^{AAoA} = 1.61$	
			Low	$\mu_d^{AAoA} = 1.01, \sigma_d^{AAoA} = 1.58$	
	EAoD	Gaussian	Static scatterer	High	$\mu_s^{EAoD} = 0.06, \sigma_s^{EAoD} = 0.09$
				Medium	$\mu_s^{EAoD} = 0.07, \sigma_s^{EAoD} = 0.16$
				Low	$\mu_s^{EAoD} = 0.06, \sigma_s^{EAoD} = 0.10$
		Dynamic scatterer	High	$\mu_d^{EAoD} = 0.57, \sigma_d^{EAoD} = 0.62$	
			Medium	$\mu_d^{EAoD} = 0.66, \sigma_d^{EAoD} = 0.59$	
			Low	$\mu_d^{EAoD} = 0.80, \sigma_d^{EAoD} = 0.56$	
	EAoA	Gaussian	Static scatterer	High	$\mu_s^{EAoA} = 0.06, \sigma_s^{EAoA} = 0.09$
				Medium	$\mu_s^{EAoA} = 0.07, \sigma_s^{EAoA} = 0.16$
				Low	$\mu_s^{EAoA} = 0.06, \sigma_s^{EAoA} = 0.10$
		Dynamic scatterer	High	$\mu_d^{EAoA} = 0.57, \sigma_d^{EAoA} = 0.62$	
			Medium	$\mu_d^{EAoA} = 0.66, \sigma_d^{EAoA} = 0.59$	
			Low	$\mu_d^{EAoA} = 0.80, \sigma_d^{EAoA} = 0.56$	
Power-Delay	Exponential	Static scatterer	High	$\xi_s = 7.75 \times 10^6, \eta_s = 30.28, \sigma_{E,s} = 9.81$	
			Medium	$\xi_s = 8 \times 10^6, \eta_s = 31.90, \sigma_{E,s} = 11.10$	
			Low	$\xi_s = 10 \times 10^6, \eta_s = 29.38, \sigma_{E,s} = 9.71$	
		Dynamic scatterer	High	$\xi_d = 4.54 \times 10^6, \eta_d = 31.08, \sigma_{E,d} = 9.60$	
			Medium	$\xi_d = 1.50 \times 10^6, \eta_d = 32.80, \sigma_{E,d} = 10.90$	
			Low	$\xi_d = 4.47 \times 10^6, \eta_d = 30.17, \sigma_{E,d} = 8.72$	

[6] simply assumed that the numbers of static scatterers and dynamic scatterers obey the Gaussian distribution and the uniform distribution, respectively. To have a comprehensive characterization of channels for vehicular intelligent sensing-communication integration, the numbers of static and dynamic scatterers are adequately explored. For generality, two new scatterer number parameters  $N_s^{c1,c3}(t)$  and  $M_s^{c1,c3}(t)$ , which represent the ratios of static and dynamic scatterer numbers to transceiver distance in a certain communication link, e.g., Car1 is the Tx and Car3 is the Rx, are introduced and written by

$$N_s^{c1,c3}(t) = \frac{I^{c1,c3}(t)}{\|\mathbf{T}^{c1,c3}(t) - \mathbf{R}^{c1,c3}(t)\|} \quad (5)$$

$$M_s^{c1,c3}(t) = \frac{J^{c1,c3}(t)}{\|\mathbf{T}^{c1,c3}(t) - \mathbf{R}^{c1,c3}(t)\|} \quad (6)$$

where  $I^{c1,c3}(t)$  and  $J^{c1,c3}(t)$  are the numbers of static and dynamic scatterers in the communication link between Car1, i.e., Tx, and Car3, i.e., Rx.  $\mathbf{T}^{c1,c3}(t)$  and  $\mathbf{R}^{c1,c3}(t)$  are the positions of Car1 and Car3. Moreover, we compute the number parameters of static and dynamic scatterers for each communication link at each snapshot. Figs. 3(a)–(c) give the cumulative distribution functions (CDFs) of all number parameters of static and dynamic scatterers under high, medium, and low VTDs, respectively. It can be observed that the CDFs of static and dynamic scatterer number parameters can fit well with the Logistic distribution. The CDF of the Logistic distribution for

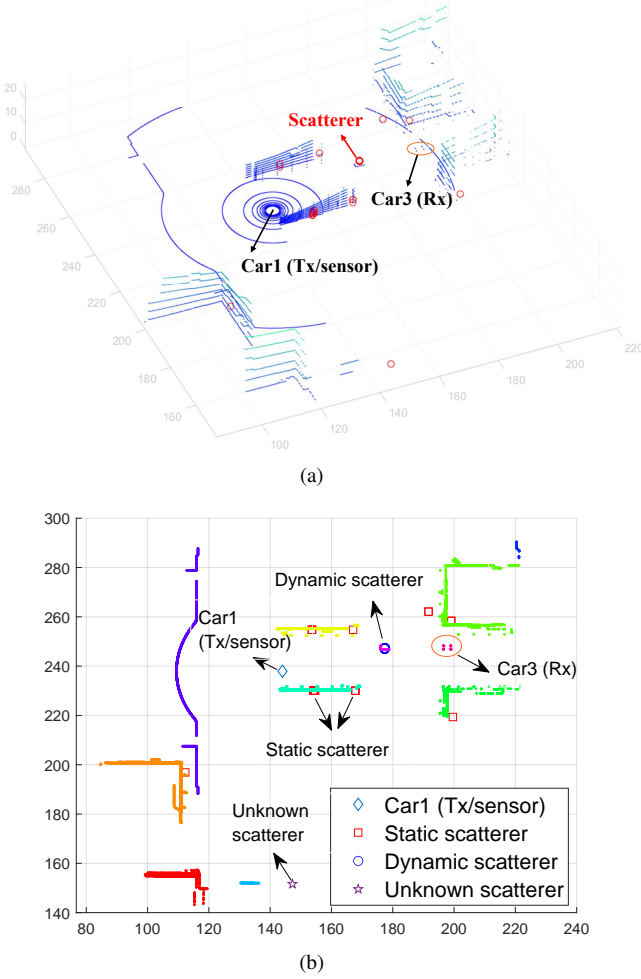


Fig. 2. LiDAR point clouds and scatterers under medium VTD at initial time. (a) LiDAR point clouds and scatterers before ground segmentation from 3D perspective. (b) LiDAR point clouds and scatterers after DBSCAN clustering from the BEV perspective.

static/dynamic scatterers is given by

$$F_{s/d}^{s,L}(x) = \frac{1}{1 + e^{-(x - \mu_{s/d}^{s,L})/\gamma_{s/d}^{s,L}}} \quad (7)$$

where  $\mu_{s/d}^{s,L}$  is the mean and  $\gamma_{s/d}^{s,L}$  is the scale parameter of the Logistic distribution for static/dynamic scatterers. In Table II and Fig. 3, for the dynamic scatterer, the mean and variance of its number parameter increase as the VTD increases. This is because that the increase in the number of dynamic vehicles around the transceiver leads to the increase in the number of dynamic scatterers. Unlike dynamic scatterers, as the VTD increases, the mean and variance of static scatterer number parameter increase first and then decrease. This phenomenon is explained that, with the increase of vehicles, the environment tends to be a rich scattering environment (SE), i.e., there are more propagation paths. In this case, static components increase, leading to the increase in the number of static scatterers. However, as the number of vehicles further increases, the static component is significantly blocked by vehicles, leading to the decrease in the number of static scatterers.

To further investigate channel characteristics for vehicular intelligent sensing-communication integration, the scatterers

are clustered to explore the statistical distribution of cluster number. Similarly, two new cluster number parameters  $N_c^{c1,c3}(t)$  and  $M_c^{c1,c3}(t)$ , which represent the ratios of static and dynamic clusters numbers to the distance between Car1, i.e., Tx, and Car3, i.e., Rx, are introduced. We calculate the number parameters of static and dynamic clusters for each communication link at each snapshot. Figs. 3(d)–(f) present the CDFs of all number parameters of static and dynamic clusters under high, medium, and low VTDs, respectively. The CDF of the Logistic distribution for static/dynamic clusters can be written as

$$F_{s/d}^{c,L}(x) = \frac{1}{1 + e^{-(x - \mu_{s/d}^{c,L})/\gamma_{s/d}^{c,L}}} \quad (8)$$

where  $\mu_{s/d}^{c,L}$  is the mean and  $\gamma_{s/d}^{c,L}$  is the scale parameter of the Logistic distribution for static/dynamic clusters. From Table II and Fig. 3, it can be seen that the observation of static/dynamic cluster number parameters is similar to that of static/dynamic scatterer number parameters.

### B. Distance Parameters

In the stochastic channel modeling approach, distance parameters of scatterers can be assumed to obey a certain statistical distribution. The standardized channel models in [16] and [30] assumed that distance parameters of scatterers obey the Exponential distribution, while ignored the distinction between static and dynamic scatterers. To overcome this limitation, we simultaneously explore distance characteristics of static scatterers and dynamic scatterers. To be specific, two new distance parameters  $D_i^{c1,c3}(t)$  and  $D_j^{c1,c3}(t)$  related to the  $i$ -th static scatterer and the  $j$ -th dynamic scatterer are introduced and expressed as

$$D_i^{c1,c3}(t) = \frac{\|\mathbf{T}^{c1,c3}(t) - \mathbf{S}_i^{c1,c3}(t)\| + \|\mathbf{R}^{c1,c3}(t) - \mathbf{S}_i^{c1,c3}(t)\| - \|\mathbf{T}^{c1,c3}(t) - \mathbf{R}^{c1,c3}(t)\|}{\|\mathbf{T}^{c1,c3}(t) - \mathbf{R}^{c1,c3}(t)\|} \quad (9)$$

$$D_j^{c1,c3}(t) = \frac{\|\mathbf{T}^{c1,c3}(t) - \mathbf{S}_j^{c1,c3}(t)\| + \|\mathbf{R}^{c1,c3}(t) - \mathbf{S}_j^{c1,c3}(t)\| - \|\mathbf{T}^{c1,c3}(t) - \mathbf{R}^{c1,c3}(t)\|}{\|\mathbf{T}^{c1,c3}(t) - \mathbf{R}^{c1,c3}(t)\|} \quad (10)$$

where  $\|\cdot\|$  denotes the Frobenius norm.  $\mathbf{S}_i^{c1,c3}(t)$  and  $\mathbf{S}_j^{c1,c3}(t)$  denote the positions of the  $i$ -th static scatterer and the  $j$ -th dynamic scatterer in the communication link between Car1, i.e., Tx, and Car3, i.e., Rx. Furthermore, we compute the distance parameter of each static/dynamic scatterer for each communication link at each snapshot. Figs. 4(a)–(c) show the CDFs of all distance parameters of static and dynamic scatterers under high, medium, and low VTDs, respectively. From Fig. 4, it is clear that the CDF of static scatterer distance parameters matches with the Gamma distribution. The CDF of the Gamma distribution is given by

$$F_s^G(x) = \frac{\gamma(\alpha_s^G, \beta_s^G x)}{\Gamma(\alpha_s^G)} \quad (11)$$

where  $\alpha_s^G$  is the shape parameter and  $\beta_s^G$  is the rate parameter of the Gamma distribution.  $\gamma(\cdot, \cdot)$  is the lower incomplete Gamma function and  $\Gamma(\cdot)$  is the Gamma function. Different from static scatterers, the CDF of dynamic scatterer distance parameters matches with the Rayleigh distribution. The

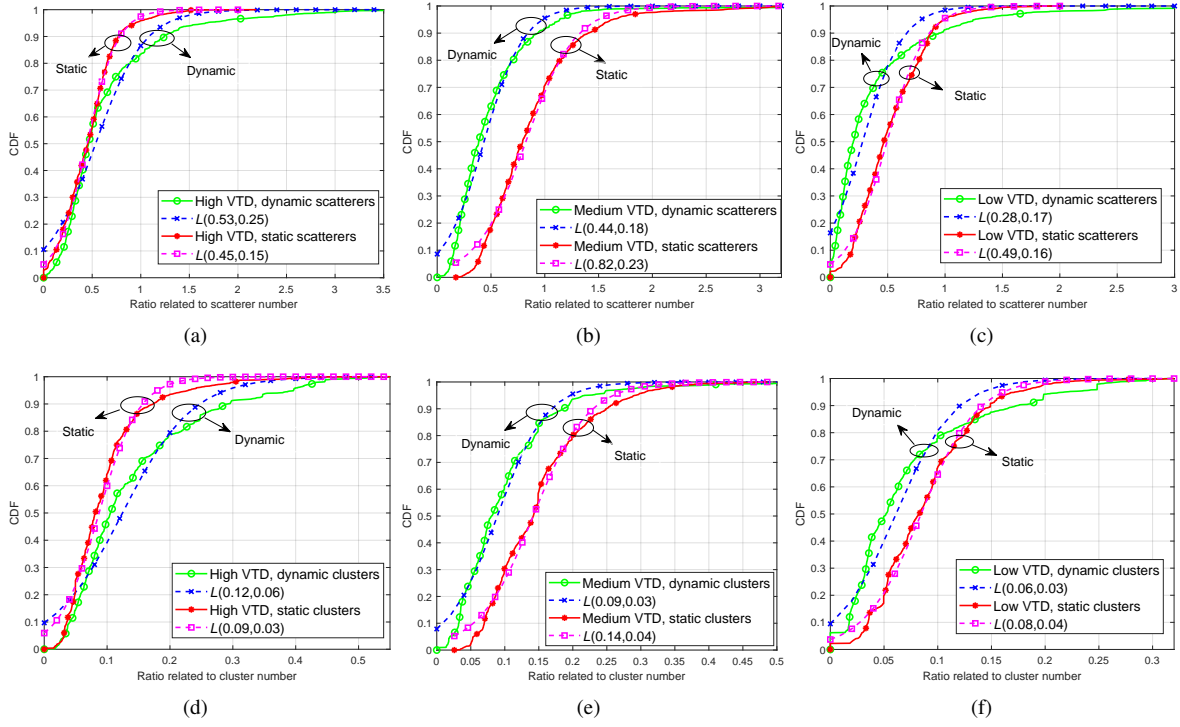


Fig. 3. CDFs of static/dynamic scatterer and cluster number parameters with the Logistic distribution fitting under different VTDs. Figs. (a)–(c) show the CDFs of scatterer number parameters under high, medium, and low VTDs, respectively. Figs. (d)–(f) show the CDFs of cluster number parameters under high, medium, and low VTDs, respectively.

CDF of the Rayleigh distribution for the dynamic scatterer distance parameter is expressed by

$$F_d^R(x) = 1 - e^{-\frac{x^2}{2(\sigma_d^R)^2}} \quad (12)$$

where  $\sigma_d^R$  is the scale parameter of the Rayleigh distribution. In Table II and Fig. 4, compared to dynamic scatterers, the distance parameter of static scatterers is larger. This is because that dynamic scatterers are mainly vehicles surrounding the transceiver, while static scatterers are mainly trees and buildings on the roadside, and they are far away from the transceiver. For the impact of VTDs, as the VTD increases, the mean and variance of dynamic scatterer distance parameters increase, whereas the mean and variance of static scatterer distance parameters increase first and then decrease. The physical reason is that there are more dynamic vehicles around the transceiver in high VTDs, where the propagation environment is more complex and the spatial distribution of dynamic scatterers is more dispersed. Also, the increase in the number of vehicles leads to a rich SE and more dispersed spatial distribution of static scatterers. Nevertheless, as the number of vehicles further increases, static components via the trees and buildings are greatly blocked by vehicles, leading to more concentrated spatial distribution of static scatterers.

### C. Angle Parameters

An in-depth understanding of angle parameters is also important for channel characterization [31]. The authors in [9] found that the angle parameters follow the Laplace distribution, while the propagation environment was limited

to two-dimensional (2D) environment. Furthermore, Yang *et al.* [32] also explored that the angle parameters follow the Laplace distribution in 3D V2V propagation environment, while disregarded the distinction between static scatterers and dynamic scatterers. Based on the sensing-communication simulation dataset in [24], the angle characteristics, including azimuth angle of departure (AAoD), azimuth angle of arrival (AAoA), elevation angle of departure (EAoD), and elevation angle of arrival (EAoA) of static and dynamic scatterers, are investigated. For clarity, we take the AAoD as an example for analysis. Two new angle parameters  $\alpha_i^{c1,c3}(t)$  and  $\alpha_j^{c1,c3}(t)$ , which represent the ratios of the AAoDs of the  $i$ -th static scatterer and the  $j$ -th dynamic scatterer to transceiver distance in the communication link between Car1, i.e., Tx, and Car3, i.e., Rx, are introduced

$$\alpha_i^{c1,c3}(t) = \frac{\gamma_i^{c1,c3}(t)}{\|\mathbf{T}^{c1,c3}(t) - \mathbf{R}^{c1,c3}(t)\|} \quad (13)$$

$$\alpha_j^{c1,c3}(t) = \frac{\gamma_j^{c1,c3}(t)}{\|\mathbf{T}^{c1,c3}(t) - \mathbf{R}^{c1,c3}(t)\|} \quad (14)$$

where  $\gamma_i^{c1,c3}(t)$  and  $\gamma_j^{c1,c3}(t)$  denote the AAoDs of the  $i$ -th static scatterer and the  $j$ -th dynamic scatterer in the communication link between Car1 and Car3. Similarly, we compute the angle parameter, i.e., AAoD, of each static/dynamic scatterer for each communication link at each snapshot. Figs. 5(a)–(c) depict the CDFs of all angle parameters, i.e., AAoDs, of static and dynamic scatterers under high, medium, and low VTDs, respectively. A close agreement between the Gaussian distribution and the corresponding CDFs is achieved. The CDF of

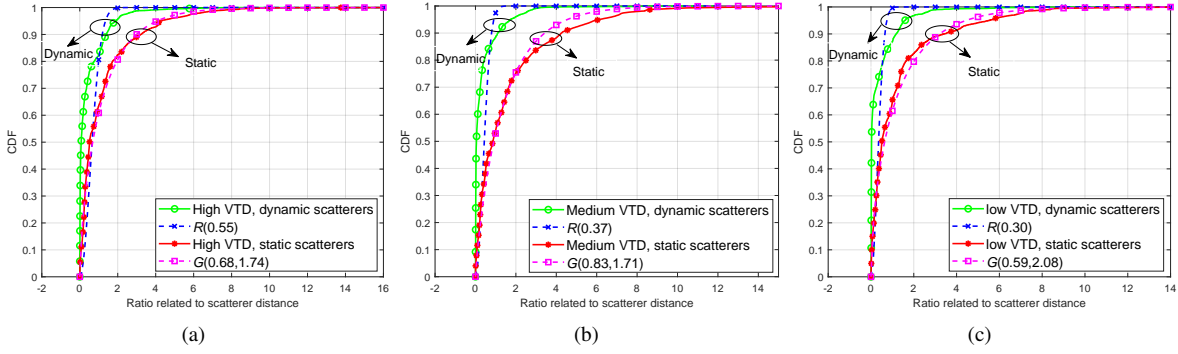


Fig. 4. CDFs of static/dynamic scatterer distance parameters with the Gamma/Rayleigh distribution fitting under different VTDs. (a) High VTD. (b) Medium VTD. (c) Low VTD.

the Gaussian distribution for AAoDs related to static/dynamic scatterers is expressed by

$$F_{s/d}^{\text{AAoD}}(x) = \frac{1}{2} \left[ 1 + \operatorname{erf} \left( \frac{x - \mu_{s/d}^{\text{AAoD}}}{\sigma_{s/d}^{\text{AAoD}} \sqrt{2}} \right) \right] \quad (15)$$

where  $\mu_{s/d}^{\text{AAoD}}$  is the mean and  $\sigma_{s/d}^{\text{AAoD}}$  is the standard deviation of the Gaussian distribution for AAoDs related to static/dynamic scatterers.  $\operatorname{erf}(\cdot)$  is the error function. Note that other static/dynamic scatterer angle parameters, i.e., AAoA  $\theta_j^{c1,c3}(t)$ , EAoD  $\beta_j^{c1,c3}(t)$ , and EAoA  $\phi_j^{c1,c3}(t)$ , also follow the Gaussian distribution and statistical values are given in Table II. It can be seen from Table II and Fig. 5 that, compared with static scatterers, dynamic scatterers have smaller variance in the horizontal angle, while larger variance in the elevation angle. This is because that the spatial distribution of dynamic scatterers is more concentrated and closer to the transceiver. Furthermore, as the VTD increases, the variance of dynamic scatterer angle parameters increases, whereas the variance of static scatterer angle parameters increases first and then decreases. The physical reason is similar to the aforementioned static/dynamic scatterer number and distance parameters.

#### D. Power-Delay Characteristics

In addition to 3D coordinates of static and dynamic scatterers, the sensing-communication simulation dataset also includes delay and power information of each path in the propagation environment. As mentioned in [33], the path power is an exponential function of the path delay. Therefore, the power  $P_k(t)$  and  $P_l(t)$  of the  $k$ -th static path and the  $l$ -th dynamic path in the communication link can be expressed by

$$P_k(t) = \exp(-\xi_s \tau_k(t) - \eta_s) 10^{-\frac{Z_s}{10}} \quad (16)$$

$$P_l(t) = \exp(-\xi_d \tau_l(t) - \eta_d) 10^{-\frac{Z_d}{10}} \quad (17)$$

where  $\xi_{s/d}$  and  $\eta_{s/d}$  are the introduced delay-related parameters of static/dynamic scatterers.  $\tau_{k/l}(t)$  is the delay of the  $k/l$ -th static/dynamic path.  $Z_s$  and  $Z_d$  obey the Gaussian distributions  $\mathcal{N}(0, \sigma_{E,s}^2)$  and  $\mathcal{N}(0, \sigma_{E,d}^2)$ , respectively. To apply the linear regression based on ordinary least squares, we transform (16) and (17) as

$$-\ln P_k(t) = \xi_s \tau_k(t) + \eta_s + \frac{\ln 10}{10} Z_s \quad (18)$$

$$-\ln P_l(t) = \xi_d \tau_l(t) + \eta_d + \frac{\ln 10}{10} Z_d. \quad (19)$$

We calculate the power and delay of each static/dynamic path at each snapshot, and then exploit the linear regression based on ordinary least squares. Table II gives the fitted parameters. Figs. 6(a)–(c) further present the fitting results under high, medium, and low VTDs, respectively, validating the accuracy of the fitted parameters. Compared to static scatterers, the power of dynamic scatterers is more sensitive to the change of delay, and thus the increase in the delay of dynamic scatterers significantly reduce their power. Furthermore, as the VTD decreases, the decrease in the dynamic scatterer power is more obvious with the increase in the delay, i.e., larger  $\xi_d$ .

#### IV. A NOVEL NON-STATIONARY AND CONSISTENT LA-GBSM

With the help of LiDAR point clouds, the statistical distributions of parameters, such as distance, angle, number, and power, related to static and dynamic scatterers under high, medium, and low VTD conditions are obtained. Furthermore, based on the obtained statistical distributions, a novel non-stationary and consistent mmWave LA-GBSM for vehicular intelligent sensing-communication integration is proposed. It is the first time that non-RF sensory information, which is intelligently processed by machine learning, is exploited to facilitate the RF channel modeling.

##### A. Framework of the Proposed LA-GBSM

The geometric representation of the proposed LA-GBSM is depicted in Fig. 7. The transceiver distance is  $D_{\text{cen}}(t_0)$  at initial time. As a result, according to Table II, the numbers  $N_s(t_0)$  and  $M_s(t_0)$  of static and dynamic scatterers are generated by the Logistic distribution. The position of the  $i/j$ -th static/dynamic scatterer is generated based on the distance  $D_i(t_0)/D_j(t_0)$  with the Gamma/Rayleigh distribution and angles, i.e., AAoDs  $\alpha_i(t_0)$  and  $\alpha_j(t_0)$ , AAoAs  $\theta_i(t_0)$  and  $\theta_j(t_0)$ , EAoDs  $\beta_i(t_0)$  and  $\beta_j(t_0)$ , and EAoAs  $\phi_i(t_0)$  and  $\phi_j(t_0)$ , with the Gaussian distribution. The generated static and dynamic scatterers are clustered via the  $K$ -Means clustering algorithm to obtain static and dynamic clusters, respectively. Note that the numbers  $N_c(t_0)$  and  $M_c(t_0)$ , i.e.,  $K$  value in the  $K$ -Means clustering algorithm, of static and dynamic clusters

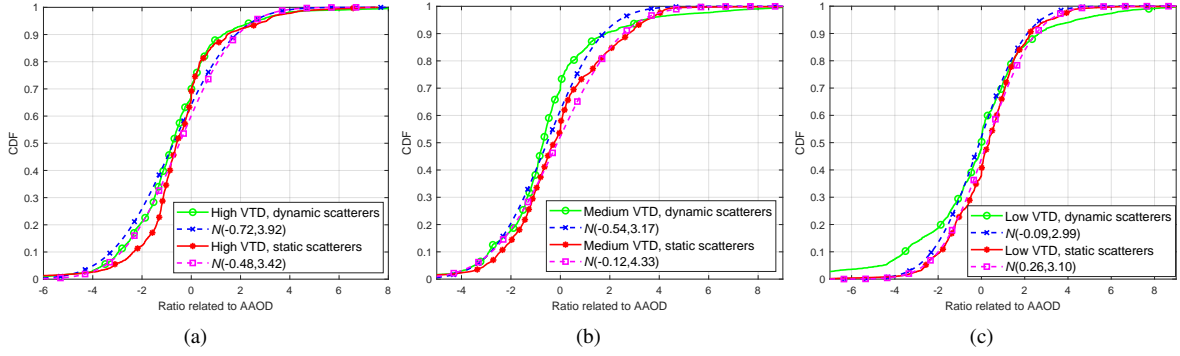


Fig. 5. CDFs of static/dynamic scatterer angle parameters, i.e., AAoD, with the Gaussian distribution fitting under different VTDs. (a) High VTD. (b) Medium VTD. (c) Low VTD.

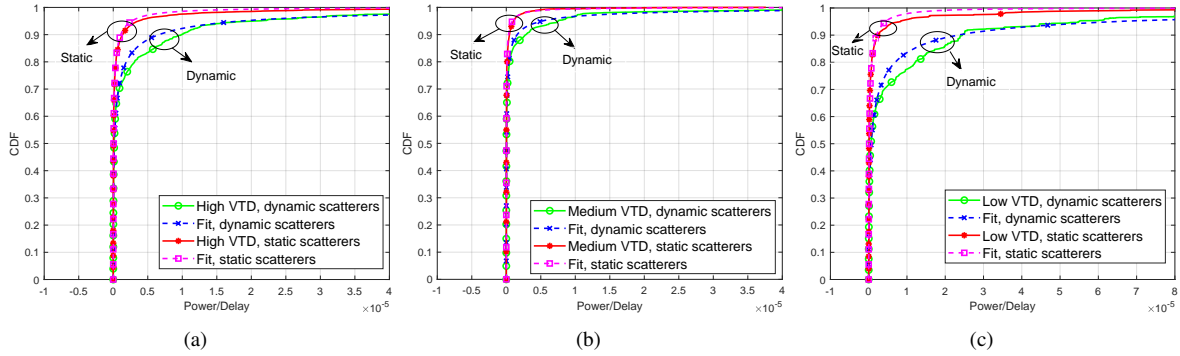


Fig. 6. CDFs of the ratios of static/dynamic scatterer power to static/dynamic scatterer delay with the Exponential expression fitting under different VTDs. (a) High VTD. (b) Medium VTD. (c) Low VTD.

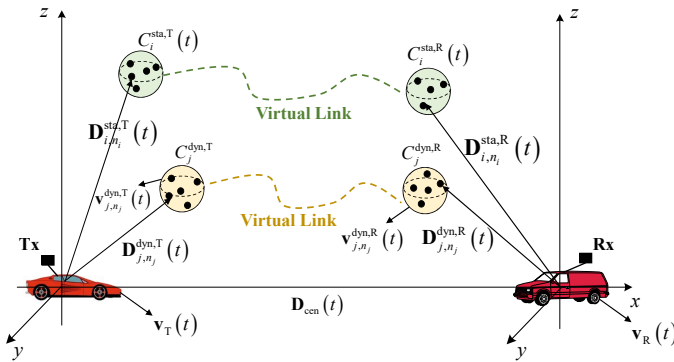


Fig. 7. Geometry of the proposed channel model for vehicular intelligent sensing-communication integration.

are also determined by the Logistic distribution according to Table II. Furthermore, we define the cluster whose centroid is closer to Tx/Rx as the Tx/Rx cluster. The Tx cluster and the Rx cluster are randomly shuffled and matched to form the twin-cluster similar to [30]. The transmission between the twin-cluster is abstracted as a virtual link, where other clusters may exist and introduce the second-order and beyond interaction. The  $i$ -th Tx/Rx static cluster and the  $j$ -th Tx/Rx dynamic cluster are represented by  $C_i^{sta,T/R}$  and  $C_j^{dyn,T/R}$ . The dynamic cluster  $C_j^{dyn,T/R}$  moves with the velocity vector  $\mathbf{v}_j^{dyn,T/R}(t)$ . The scatterer within a cluster has the same velocity vector as the cluster, which can be expressed by

$\mathbf{v}_{j,n_j}^{dyn,T/R}(t) = \mathbf{v}_j^{dyn,T/R}(t)$ . Finally, the velocity vectors of transceivers are  $\mathbf{v}_T(t)$  and  $\mathbf{v}_R(t)$ .

The complex channel gain of the line-of-sight (LoS) component can be represented as

$$h^{LoS}(t) = Q(t) \exp \left[ j2\pi \int_{t_0}^t f^{LoS}(t) dt + j\varphi^{LoS}(t) \right] \quad (20)$$

where  $T_0$  denotes the observation time interval and  $Q(t)$  represents a rectangular window function [34], which can be given by

$$Q(t) = \begin{cases} 1, & t_0 \leq t \leq T_0, \\ 0, & \text{otherwise.} \end{cases} \quad (21)$$

In addition, the Doppler frequency  $f^{LoS}(t)$ , phase shift  $\varphi^{LoS}(t)$ , as well as delay  $\tau^{LoS}(t)$  are calculated as  $f^{LoS}(t) = \frac{1}{\lambda} \frac{\langle \mathbf{D}_{cen}(t), \mathbf{v}_R(t) - \mathbf{v}_T(t) \rangle}{\|\mathbf{D}_{cen}(t)\|}$ ,  $\varphi^{LoS}(t) = \varphi_0 + \frac{2\pi}{\lambda} \|\mathbf{D}_{cen}(t)\|$ , and  $\tau^{LoS}(t) = \frac{\|\mathbf{D}_{cen}(t)\|}{c}$ , where  $\langle \cdot, \cdot \rangle$ ,  $\varphi_0$ ,  $\lambda$ , and  $c$  represent the inner product, initial phase shift, carrier wavelength, and speed of light.  $\mathbf{D}_{cen}(t)$  is the transceiver distance at time  $t$  and is given as

$$\mathbf{D}_{cen}(t) = \mathbf{D}_{cen}(t_0) + \int_{t_0}^t \mathbf{v}_R(t) dt - \int_{t_0}^t \mathbf{v}_T(t) dt. \quad (22)$$

Continuously arbitrary vehicular movement trajectories (VMTs) of transceivers and dynamic clusters are captured similar to our previous work in [15].

For non-LoS (NLoS) components, the complex channel gain via the static twin-cluster  $C_i^{\text{sta},\text{T/R}}$  by the  $n_i$ -th static scatterer can be written by

$$h_{i,n_i}^{\text{sta}}(t) = Q(t) \sqrt{P_{i,n_i}^{\text{sta}}(t)} \times \exp \left\{ j2\pi \left[ \int_{t_0}^t f_{i,n_i}^{\text{sta},\text{T}}(t) dt + \int_{t_0}^t f_{i,n_i}^{\text{sta},\text{R}}(t) dt \right] + j\varphi_{i,n_i}^{\text{sta}}(t) \right\} \quad (23)$$

where  $P_{i,n_i}^{\text{sta}}(t)$  represents the normalized static scatterer power, which can be determined according to Table II. The Doppler frequency of the static cluster at Tx/Rx is computed by

$$f_{i,n_i}^{\text{sta},\text{T/R}}(t) = \frac{1}{\lambda} \frac{\langle \mathbf{D}_{i,n_i}^{\text{sta},\text{T/R}}(t), \mathbf{v}_{\text{T/R}}(t) \rangle}{\|\mathbf{D}_{i,n_i}^{\text{sta},\text{T/R}}(t)\|},$$

where  $\mathbf{D}_{i,n_i}^{\text{sta},\text{T/R}}(t)$  denotes the distance between the Tx/Rx and the  $n_i$ -th static scatterer via the static cluster  $C_i^{\text{sta},\text{T/R}}$ . The corresponding

delay is computed by  $\tau_{i,n_i}^{\text{sta}}(t) = \frac{\|\mathbf{D}_{i,n_i}^{\text{sta},\text{T}}(t)\| + \|\mathbf{D}_{i,n_i}^{\text{sta},\text{R}}(t)\|}{c} + \tilde{\tau}_i(t)$ , where  $\tilde{\tau}_i(t)$  represents the abstracted delay of the virtual link between the static twin-cluster  $C_i^{\text{sta},\text{T/R}}$  and follows the Exponential distribution [35]. The phase shift of the component via the  $n_i$ -th static scatterer within the static twin-cluster  $C_i^{\text{sta},\text{T/R}}$  is given by  $\varphi_{i,n_i}^{\text{sta}}(t) = \varphi_0 + \frac{2\pi}{\lambda} \left[ \|\mathbf{D}_{i,n_i}^{\text{sta},\text{T}}(t)\| + \|\mathbf{D}_{i,n_i}^{\text{sta},\text{R}}(t)\| + c\tilde{\tau}_i(t) \right]$ . Also, the complex channel gain for NLoS components via the dynamic twin-cluster  $C_j^{\text{dyn},\text{T/R}}$  by the  $n_j$ -th dynamic scatterer is given as

$$h_{j,n_j}^{\text{dyn}}(t) = Q(t) \sqrt{P_{j,n_j}^{\text{dyn}}(t)} \times \exp \left\{ j2\pi \left[ \int_{t_0}^t f_{j,n_j}^{\text{dyn},\text{T}}(t) dt + \int_{t_0}^t f_{j,n_j}^{\text{dyn},\text{R}}(t) dt \right] + j\varphi_{j,n_j}^{\text{dyn}}(t) \right\} \quad (24)$$

where  $P_{j,n_j}^{\text{dyn}}(t)$  denotes the normalized dynamic scatterer power, which can be properly determined according to Table II. The Doppler frequency of the dynamic cluster at Tx/Rx is computed by  $f_{j,n_j}^{\text{dyn},\text{T/R}}(t) =$

$$\frac{1}{\lambda} \frac{\langle \mathbf{D}_{j,n_j}^{\text{dyn},\text{T/R}}(t), \mathbf{v}_{\text{T/R}}(t) - \mathbf{v}_{j,n_j}^{\text{dyn},\text{T/R}}(t) \rangle}{\|\mathbf{D}_{j,n_j}^{\text{dyn},\text{T/R}}(t)\|},$$

where  $\mathbf{D}_{j,n_j}^{\text{dyn},\text{T/R}}(t)$  is the distance between the Tx/Rx and the  $n_j$ -th dynamic scatterer via the dynamic cluster  $C_j^{\text{dyn},\text{T/R}}$ . The corresponding delay

is computed by  $\tau_{j,n_j}^{\text{dyn}}(t) = \frac{\|\mathbf{D}_{j,n_j}^{\text{dyn},\text{T}}(t)\| + \|\mathbf{D}_{j,n_j}^{\text{dyn},\text{R}}(t)\|}{c} + \tilde{\tau}_j(t)$ , where  $\tilde{\tau}_j(t)$  represents the abstracted delay of the virtual link between the dynamic twin-cluster  $C_j^{\text{dyn},\text{T/R}}$  and also follows the Exponential distribution. The phase shift of the component via the  $n_j$ -th dynamic scatterer within the dynamic twin-cluster  $C_j^{\text{dyn},\text{T/R}}$  can be expressed as  $\varphi_{j,n_j}^{\text{dyn}}(t) = \varphi_0 +$

$$\frac{2\pi}{\lambda} \left[ \|\mathbf{D}_{j,n_j}^{\text{dyn},\text{T}}(t)\| + \|\mathbf{D}_{j,n_j}^{\text{dyn},\text{R}}(t)\| + c\tilde{\tau}_j(t) \right].$$

The complex channel gain of ground reflection component is written as

$$h^{\text{GR}}(t) = Q(t) \sqrt{P^{\text{GR}}(t)} \times \exp \left\{ j2\pi \left[ \int_{t_0}^t f^{\text{GR},\text{T}}(t) dt + \int_{t_0}^t f^{\text{GR},\text{R}}(t) dt \right] + j\varphi^{\text{GR}}(t) \right\} \quad (25)$$

where  $P^{\text{GR}}(t)$ ,  $f^{\text{GR},\text{T/R}}(t)$ , and  $\varphi^{\text{GR}}(t)$  denote the power, Doppler frequency at Tx/Rx, and phase shift of ground reflection component, respectively. In addition,  $\tau^{\text{GR}}(t)$  is the delay of ground reflection component. The power  $P^{\text{GR}}(t)$ , Doppler frequency at Tx/Rx  $f^{\text{GR},\text{T/R}}(t)$ , phase shift  $\varphi^{\text{GR}}(t)$ , and delay  $\tau^{\text{GR}}(t)$  can be computed similar to our previous work in [15].

Overall, the channel impulse response (CIR) of the proposed LA-GBSM for vehicular intelligent sensing-communication integration can be expressed by (26), shown at the top of the next page.  $\Omega(t)$  represents the Ricean factor.  $\eta^{\text{GR}}(t)$ ,  $\eta^{\text{sta}}(t)$ , and  $\eta^{\text{dyn}}(t)$  represent the power ratios of the ground reflection component, component via static clusters, and component via dynamic clusters and have  $\eta^{\text{GR}}(t) + \eta^{\text{sta}}(t) + \eta^{\text{dyn}}(t) = 1$ . In the derived CIR, the key channel-related parameters, including number, distance, angle, and power, under high, medium, and low VTD conditions are determined according to Table II.

## B. Capturing of Channel Non-Stationarity and Consistency

Channel non-stationarity is a typical channel characteristic and channel consistency is an inherent channel physical feature. As mentioned in [4], channel non-stationarity and channel consistency need to be captured in high-mobility V2V communication channels under the mmWave frequency band. Based on the obtained statistical distributions, a new VR-based algorithm in consideration of newly generated static/dynamic clusters is developed to capture channel non-stationarity and consistency in the time domain, i.e., time non-stationarity and consistency. Moreover, a frequency-dependent factor is introduced to model channel non-stationarity in the frequency domain, i.e., frequency non-stationarity.

Currently, the VR method is widely used in channel modeling [36]. In the VR method, clusters are visible and contribute to channel realization only if they are within the VR. As the VR and clusters move, the visible cluster set smoothly changes, and thus time non-stationarity and consistency are captured. To mimic smooth static/dynamic cluster time evolution in channels for vehicular intelligent sensing-communication integration, a new VR-based algorithm under high, medium, and low VTDs is developed based on the obtained statistical distribution of distance parameters. The VR is set to the 3D ellipsoid with the transceiver as the focus. For the VR, i.e., 3D ellipsoid, assigned to the static/dynamic cluster, the minor axis  $2b^{\text{sta}/\text{dyn}}(t)$  and the focal length  $2c^{\text{sta}/\text{dyn}}(t)$  are equal to the distance  $D_{\text{cen}}(t)$  between transceivers, which can be calculated by the positions of transceivers. Meanwhile, the major axis  $2a^{\text{sta}/\text{dyn}}(t)$  is equal to the sum of the distances from the static/dynamic cluster to transceivers and is computed based on the obtained statistical distribution of distance parameters, as listed in Table II. Then, a visibility factor  $\epsilon^{\text{sta}/\text{dyn}}$  is introduced to determine the major axis  $2a^{\text{sta}/\text{dyn}}(t)$  of VR assigned to static/dynamic clusters. For dynamic clusters, based on the CDF of the Rayleigh distribution of their distance parameters, the major axis  $2a^{\text{dyn}}(t)$  of VR is computed by

$$1 - \exp \left( - \frac{\left( \frac{2a^{\text{dyn}}(t) - D_{\text{cen}}(t)}{D_{\text{cen}}(t)} \right)^2}{2\sigma_d^{\text{R}^2}} \right) = \epsilon^{\text{dyn}}. \quad (27)$$

Then, the major axis  $2a^{\text{dyn}}(t)$  of VR can be computed by

$$2a^{\text{dyn}}(t) = \sqrt{-2\sigma_d^{\text{R}^2} \ln(1 - \epsilon^{\text{dyn}})} D_{\text{cen}}(t) + D_{\text{cen}}(t). \quad (28)$$

$$\begin{aligned}
h(t, \tau) = & \underbrace{\sqrt{\frac{\Omega(t)}{\Omega(t)+1}} h^{\text{LoS}}(t) \delta(\tau - \tau^{\text{LoS}}(t))}_{\text{LoS}} + \underbrace{\sqrt{\frac{\eta^{\text{GR}}(t)}{\Omega(t)+1}} h^{\text{GR}}(t) \delta(\tau - \tau^{\text{GR}}(t))}_{\text{Ground Reflection}} \\
& + \underbrace{\sum_{i=1}^{N_c(t)} \sum_{n_i=1}^{N_s(t)} \sqrt{\frac{\eta^{\text{sta}}(t)}{\Omega(t)+1}} h_{i,n_i}^{\text{sta}}(t) \delta(\tau - \tau_{i,n_i}^{\text{sta}}(t))}_{\text{NLoS}} + \underbrace{\sum_{j=1}^{M_c(t)} \sum_{n_j=1}^{M_s(t)} \sqrt{\frac{\eta^{\text{dyn}}(t)}{\Omega(t)+1}} h_{j,n_j}^{\text{dyn}}(t) \delta(\tau - \tau_{j,n_j}^{\text{dyn}}(t))}_{\text{NLoS}}. \tag{26}
\end{aligned}$$

Unlike dynamic clusters, for static clusters, based on the CDF of the Gamma distribution of their distance parameters, the major axis  $2a^{\text{sta}}(t)$  of VR can be computed by

$$\frac{1}{\Gamma(\alpha_s^G)} \gamma \left( \alpha_s^G, \beta_s^G \left( \frac{2a^{\text{sta}}(t) - D_{\text{cen}}(t)}{D_{\text{cen}}(t)} \right) \right) = \epsilon^{\text{sta}}. \tag{29}$$

Since there is no closed-form solution for the major axis  $2a^{\text{sta}}(t)$ , we calculate the numerical solution. Therefore, the VRs assigned to static and dynamic clusters are the 3D ellipsoids determined by the precise RT-based communication data, and static and dynamic clusters have different and time-varying VRs. Since the statistical values  $\sigma_d^R$ ,  $\alpha_s^G$ , and  $\beta_s^G$ , as listed in Table II, include high, medium, and low VTDs, the VRs assigned to static and dynamic clusters also consider high, medium, and low VTDs. With the help of VRs assigned to static and dynamic clusters, the numbers  $N_c^L(t)$  and  $M_c^L(t)$  of visible static and dynamic clusters can be determined.

Based on the derived statistical distribution of number parameters, the developed algorithm further models newly generated static/dynamic clusters. We take the static cluster as an example. For a certain distance  $D_{\text{cen}}(t)$  between Tx and Rx at time  $t$ , the number parameter  $N_c^L(t)$  related to static clusters is randomly generated via the Logistic distribution with the statistical values as listed in Table II. If the value  $N_c^L(t)$  is greater than the number  $N_c^v(t)$  of visible static clusters, the number of newly generated static clusters is given by

$$N_c^{\text{new}}(t) = N_c^L(t) - N_c^v(t). \tag{30}$$

In this case, there are  $N_c(t) = N_c^L(t)$  static clusters that contribute to channel realization. On the contrary, if the value  $N_c^L(t)$  is less than the number  $N_c^v(t)$  of visible static clusters, the number of newly generated static clusters is  $N_c^{\text{new}}(t) = 0$  and there are  $N_c(t) = N_c^v(t)$  static clusters that contribute to channel realization. Note that the determination of newly generated dynamic clusters has the same steps as that of newly generated static clusters. Consequently, the numbers of newly generated static and dynamic clusters are determined via the statistical distribution of cluster number parameters. Then, the parameters of newly generated static and dynamic clusters are randomly generated according to Table II. In Algorithm 1, the pseudo code of the developed algorithm is given.

The use of mmWave technology results in the necessity of capturing frequency non-stationarity [4]. To this aim, a frequency-dependent factor is introduced and used to the time-varying transfer function (TVTF). The TVTF is derived by

---

### Algorithm 1 A Novel VR-Based Algorithm with Newly Generated Static and Dynamic Clusters

---

```

1: while  $t < T_{\text{end}}$  do
2:   Determine 3D ellipsoid for static cluster via Gamma distribution;
3:   for each static cluster  $i \in [1, N_c(t)]$  do
4:     if Static cluster is within 3D ellipsoid then
5:       Visible static cluster that contributes to CIR;
6:     else
7:       Invisible static cluster that cannot contribute to CIR;
8:     end if
9:   end for
10:  Determine 3D ellipsoid for dynamic cluster via Rayleigh distribution;
11:  for each dynamic cluster  $j \in [1, M_c(t)]$  do
12:    if Dynamic cluster is within 3D ellipsoid then
13:      Visible dynamic cluster that contributes to CIR;
14:    else
15:      Invisible dynamic cluster that cannot contribute to CIR;
16:    end if
17:  end for
18:  Randomly generate number parameter  $N_c^L(t)$  for static cluster via
  Logistic distribution;
19:  if  $N_c^L(t) > N_c^v(t)$  then
20:    Generated static cluster number  $N_c^{\text{new}}(t) = N_c^L(t) - N_c^v(t)$ ;
21:  else
22:    Generated static cluster number  $N_c^{\text{new}}(t) = 0$ ;
23:  end if
24:  Randomly generate number parameter  $M_c^L(t)$  for dynamic cluster via
  Logistic distribution;
25:  if  $M_c^L(t) > M_c^v(t)$  then
26:    Generated dynamic cluster number  $M_c^{\text{new}}(t) = M_c^L(t) - M_c^v(t)$ ;
27:  else
28:    Generated dynamic cluster number  $M_c^{\text{new}}(t) = 0$ ;
29:  end if
30:  Randomly generate parameters of generated static and dynamic clusters
  according to Table II;
31:   $t = t + \Delta t$ ;
32: end while

```

---

using the Fourier transform to CIR  $h(t, \tau)$  in respect of delay  $\tau$ , which is written by

$$H'(t, f) = \int_{-\infty}^{\infty} h(t, \tau) \exp(-j2\pi f\tau) d\tau. \tag{31}$$

To capture the frequency-dependent path gain, the introduced frequency-dependent factor is applied to the TVTF, which is expressed as (32), shown at the top of the next page.  $\chi$  is a frequency-dependent parameter that is dependable on the environment [37]. With the aid of the frequency-dependent factor, the frequency-dependent path gain is imitated, thus modeling frequency non-stationarity.

## V. CHANNEL STATISTICAL PROPERTIES

Key statistical properties of channels for vehicular intelligent sensing-communication integration are derived.

$$\begin{aligned}
H(t, f) = & \underbrace{\sqrt{\frac{\Omega(t)}{\Omega(t)+1}} h^{\text{LoS}}(t) \exp[-j2\pi f \tau^{\text{LoS}}(t)]}_{\text{LoS}} + \underbrace{\sqrt{\frac{\eta^{\text{GR}}(t)}{\Omega(t)+1}} \left(\frac{f}{f_c}\right)^\chi h^{\text{GR}}(t) \exp[-j2\pi f \tau^{\text{GR}}(t)]}_{\text{Ground Reflection}} \\
& + \underbrace{\sqrt{\frac{\eta^{\text{sta}}(t)}{\Omega(t)+1}} \left(\frac{f}{f_c}\right)^\chi \sum_{i=1}^{N_c(t)} \sum_{n_i=1}^{N_s(t)} h_{i,n_i}^{\text{sta}}(t) \exp[-j2\pi f \tau_{i,n_i}^{\text{sta}}(t)] + \sqrt{\frac{\eta^{\text{dyn}}(t)}{\Omega(t)+1}} \left(\frac{f}{f_c}\right)^\chi \sum_{j=1}^{M_c(t)} \sum_{n_j=1}^{M_s(t)} h_{j,n_j}^{\text{dyn}}(t) \exp[-j2\pi f \tau_{j,n_j}^{\text{dyn}}(t)]}_{\text{NLoS}} \quad (32)
\end{aligned}$$

### A. Time-Frequency Correlation Function

Based on the TVTF, the TF-CF is computed by

$$\xi(t, f; \Delta t, \Delta f) = \mathbb{E}[H^*(t, f)H(t + \Delta t, f + \Delta f)] \quad (33)$$

where  $\mathbb{E}[\cdot]$  and  $(\cdot)^*$  represent the expectation operation and complex conjugate operation, respectively. Moreover, the TF-CFs of LoS components, ground reflection components, and NLoS components via static and dynamic clusters are given by (34) with (35)–(37), shown at the top of the next page. Based on the TF-CF, the time auto-correlation function (TACF) and the frequency correlation function (FCF) can be derived by setting  $\Delta f = 0$  and  $\Delta t = 0$ , respectively.

### B. Doppler Power Spectral Density

By taking the Fourier transfer of the derived TACF, the DPSD can be expressed by

$$\Theta(t; f_D) = \int_{-\infty}^{+\infty} \xi(t; \Delta t) e^{-j2\pi f_D \Delta t} d(\Delta t) \quad (38)$$

where  $\xi(t; \Delta t)$  is the TACF and  $f_D$  is the Doppler frequency. The derived time-varying DPSD indicates the time-varying characteristic of the proposed LA-GBSM for vehicular intelligent sensing-communication integration.

## VI. SIMULATION RESULTS AND ANALYSIS

Key channel statistical properties are simulated and compared with the accurate RT-based results. The carrier frequency is  $f_c = 28$  GHz with 2 GHz communication bandwidth. The numbers of antennas at Tx and Rx are  $M_T = M_R = 1$ . The azimuth and elevation angles at Tx and Rx sides are  $\phi_T^E = \phi_R^E = \pi/4$ ,  $\theta_T^A = \pi/3$ , and  $\theta_R^A = 3\pi/4$ . Delays of virtual links  $\tilde{\tau}_i(t)$  and  $\tilde{\tau}_j(t)$  obey the Exponential distribution with the mean and variance 80 ns and 15 ns. The environment-dependent factor is  $\chi = 1.35$  [37]. Unless otherwise stated, the aforementioned parameter remains unchanged.

### A. Model Simulation

Fig. 8 shows the absolute normalized TACFs under high, medium, and low VTDs at  $t = 0$  s and  $t = 2$  s. In Fig. 8, TACFs depend on the time instant as well as the time separation, and hence time non-stationarity is characterized. Moreover, the TACF significantly decreases as the VTD increases. This is because that, as the number of mobile vehicles increases, the channels are more complex and dynamic, and the temporal correlation is lower.

Fig. 9 depicts absolute normalized FCFs under frequencies  $f = 27$  GHz,  $f = 28$  GHz, and  $f = 29$  GHz at the

medium VTD. It can be observed from Fig. 9 that FCFs are dependable on the frequency and the frequency separation, demonstrating frequency non-stationarity of the proposed LA-GBSM. Furthermore, compared to 27 GHz, the FCF under higher frequency is lower. This phenomenon can be explained that channels at higher frequency are more complex and thus have lower frequency correlation.

### B. Model Verification

Aiming at verifying the generality of the proposed LA-GBSM, we obtain the RT-based CIR collected in Wireless InSite [21] and the scenario is shown in Fig. 1. Note that the method of comparing simulation results of the proposed channel model with RT-based results to verify the generality of the proposed channel model is widely used.

The RT-based CIR under the high VTD is processed to obtain the RT-based DPSD, which is compared with the simulated DPSDs under high, medium, and low VTDs in Fig. 10. The close match between the RT-based DPSD and the simulated DPSD under the high VTD is achieved. Moreover, compared to low VTDs, the distributions of DPSDs under high and medium VTDs are flatter. This phenomenon is explained that the received power in the high VTD tends to come from mobile vehicles around the transceiver over all directions.

In low VTDs, the RT-based CIR is further processed to obtain the RT-based TACF. In Fig. 11, the RT-based TACF is compared with the TACF of the model solely distinguishing static/dynamic scatterers, the TACF of the model with the parameter obeying the distribution derived in the standardized model, e.g., [16], and the TACF of the model under time inconsistency. To imitate time inconsistency, the birth-death process method is used to mimic the appearance and disappearance of clusters. It can be seen that, only the simulated TACF with the parameter obeying the distribution derived in the proposed model under time consistency can fit the RT-based TACF well. For the simulated TACF under time inconsistency, the smooth channel evolution in the time domain is ignored and the channel correlation at adjacent moments is underestimated, hence exhibiting lower TACF. For the model solely distinguishing static/dynamic scatterers and the model with the parameter obeying the distribution derived in the standardized model, their TACFs cannot fit well with the RT-based TACF as statistical distributions of parameters related to static/dynamic scatterers are not modeled accurately.

## VII. CONCLUSIONS

This paper has developed a novel channel modeling approach, i.e., LA-GBSM. Based on the developed LA-GBSM

$$\xi(t, f; \Delta t, \Delta f) = \xi^{\text{LoS}}(t, f; \Delta t, \Delta f) + \xi^{\text{GR}}(t, f; \Delta t, \Delta f) + \xi^{\text{NLoS}}(t, f; \Delta t, \Delta f) \quad (34)$$

$$\xi^{\text{LoS}}(t, f; \Delta t, \Delta f) = \sqrt{\frac{\Omega(t)\Omega(t+\Delta t)}{(\Omega(t)+1)(\Omega(t+\Delta t)+1)}} h^{\text{LoS}*}(t) h^{\text{LoS}}(t+\Delta t) \exp \left[ j2\pi f \tau^{\text{LoS}}(t) - (f+\Delta f) \tau^{\text{LoS}}(t+\Delta t) \right] \quad (35)$$

$$\xi^{\text{GR}}(t, f; \Delta t, \Delta f) = \sqrt{\frac{\eta^{\text{GR}}(t)\eta^{\text{GR}}(t+\Delta t)}{(\Omega(t)+1)(\Omega(t+\Delta t)+1)}} h^{\text{GR}*}(t) h^{\text{GR}}(t+\Delta t) \exp \left[ j2\pi f \tau^{\text{GR}}(t) - (f+\Delta f) \tau^{\text{GR}}(t+\Delta t) \right] \quad (36)$$

$$\begin{aligned} & \xi^{\text{NLoS}}(t, f; \Delta t, \Delta f) \\ &= \sqrt{\frac{\eta^{\text{sta}}(t)\eta^{\text{sta}}(t+\Delta t)}{(\Omega(t)+1)(\Omega(t+\Delta t)+1)}} \mathbb{E} \left[ \sum_{i=1}^{N_C(t)} \sum_{i'=1}^{N_C(t+\Delta t)} \sum_{n_i=1}^{N_S(t)} \sum_{n'_i=1}^{N_S(t+\Delta t)} h_{i,n_i}^{\text{sta}*}(t) h_{i',n'_i}^{\text{sta}}(t+\Delta t) \exp \left( j2\pi \tau_{i,n_i}^{\text{sta}}(t) f - (f+\Delta f) \tau_{i',n'_i}^{\text{sta}}(t+\Delta t) \right) \right] \\ &+ \sqrt{\frac{\eta^{\text{dyn}}(t)\eta^{\text{dyn}}(t+\Delta t)}{(\Omega(t)+1)(\Omega(t+\Delta t)+1)}} \mathbb{E} \left[ \sum_{j=1}^{M_C(t)} \sum_{j'=1}^{M_C(t+\Delta t)} \sum_{n_j=1}^{M_S(t)} \sum_{n'_j=1}^{M_S(t+\Delta t)} h_{j,n_j}^{\text{dyn}*}(t) h_{j',n'_j}^{\text{dyn}}(t+\Delta t) \exp \left( j2\pi \tau_{j,n_j}^{\text{dyn}}(t) f - (f+\Delta f) \tau_{j',n'_j}^{\text{dyn}}(t+\Delta t) \right) \right]. \end{aligned} \quad (37)$$

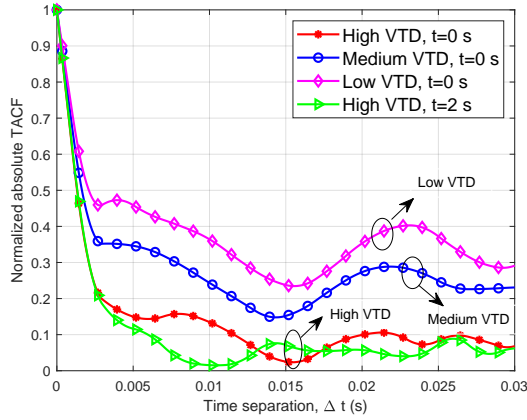


Fig. 8. TACFs under different VTDs and time instants ( $D_{\text{cen}}(t_0) = 80$  m,  $v_{\text{T}}(t_0) = 18$  m/s,  $v_{\text{R}}(t_0) = 15$  m/s,  $\bar{v}_j^{\text{dyn},\text{T}}(t_0) = 14$  m/s,  $\bar{v}_j^{\text{dyn},\text{R}}(t_0) = 15$  m/s).

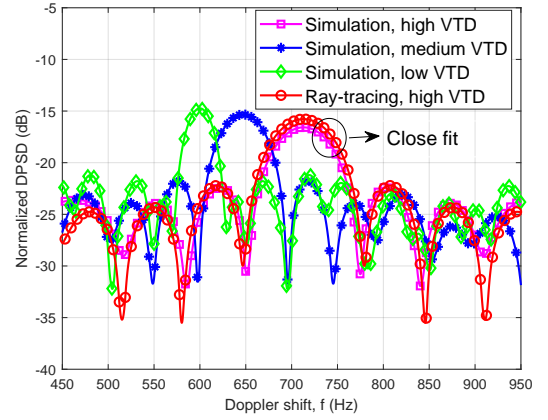


Fig. 10. Comparison of simulated DPDSs and RT-based DPDSs ( $D_{\text{cen}}(t_0) = 83.6$  m,  $v_{\text{T}}(t_0) = 10$  m/s,  $v_{\text{R}}(t_0) = 6$  m/s,  $\bar{v}_j^{\text{dyn},\text{T}}(t_0) = \bar{v}_j^{\text{dyn},\text{R}}(t_0) = 8$  m/s).

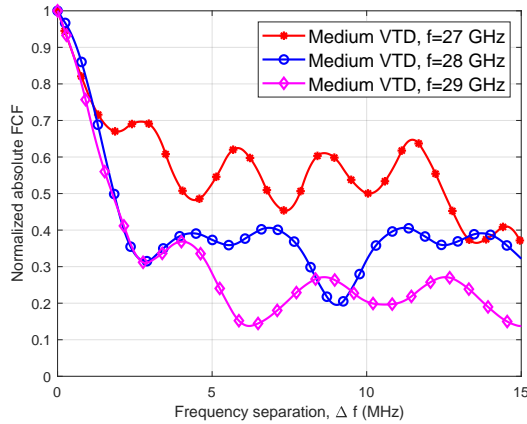


Fig. 9. FCFs under different frequencies ( $D_{\text{cen}}(t_0) = 50$  m,  $v_{\text{T}}(t_0) = 15$  m/s,  $v_{\text{R}}(t_0) = 17$  m/s,  $\bar{v}_j^{\text{dyn},\text{T}}(t_0) = \bar{v}_j^{\text{dyn},\text{R}}(t_0) = 8$  m/s,  $t = 0$  s).

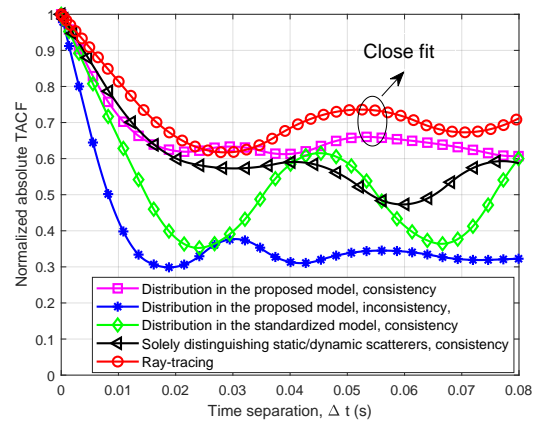


Fig. 11. Comparison of simulated TACFs and RT-based TACFs ( $D_{\text{cen}}(t_0) = 54.8$  m,  $v_{\text{T}}(t_0) = 8.33$  m/s,  $v_{\text{R}}(t_0) = 10$  m/s,  $\bar{v}_j^{\text{dyn},\text{T}}(t_0) = \bar{v}_j^{\text{dyn},\text{R}}(t_0) = 12$  m/s).

approach, a new non-stationary and consistent mmWave channel model has been proposed to support the design of vehicular intelligent sensing-communication integration systems in ITSs. The proposed LA-GBSM has been parameterized under different VTD conditions by a sensing-communication simulation dataset. The distance parameters of static and dynamic scatterers have followed the Gamma and Rayleigh

distributions, respectively. Although the number, angle, and power-delay characteristics of static and dynamic scatterers have respectively obeyed the same Logistic, Gaussian, and Exponential distributions, their statistical distribution values have shown a significant difference. Furthermore, based on the obtained statistical distribution under high, medium, and low

VTD conditions, a new VR-based algorithm in consideration of newly generated static/dynamic clusters has been developed to capture channel non-stationarity and consistency. Key channel statistics have been derived and simulated. Simulation results have shown that the time-frequency non-stationarity and time consistency have been captured. Compared to the medium and low VTD conditions, the proposed LA-GBSM for vehicular intelligent sensing-communication integration has exhibited lower temporal correlation and flatter distribution of DPSD under the high VTD condition. By comparing simulation results and RT-based results, the generality of the proposed LA-GBSM has been verified.

## REFERENCES

- [1] X. Cheng, D. Duan, S. Gao, and L. Yang, "Integrated sensing and communications (ISAC) for vehicular communication networks (VCN)," *IEEE Internet Things J.*, vol. 9, no. 23, pp. 23441–23451, Dec. 2022.
- [2] J. Wang *et al.*, "Integrated sensing and communication: Enabling techniques, applications, tools and datasets, standardization, and future directions," *IEEE Internet. Things J.*, vol. 9, no. 23, pp. 23416–23440, Dec. 2022.
- [3] X. Cheng *et al.*, "Intelligent multi-modal sensing-communication integration: Synesthesia of Machines," available on *arXiv*, 2023. [Online]. Available: <https://arxiv.org/abs/2306.14143>
- [4] X. Cheng, Z. Huang, and L. Bai, "Channel nonstationarity and consistency for beyond 5G and 6G: A survey," *IEEE Commun. Surveys Tutor.*, vol. 24, no. 3, pp. 1634–1669, third-quarter 2022.
- [5] R. He *et al.*, "Propagation channels of 5G millimeter-wave vehicle-to-vehicle communications: Recent advances and future challenges," *IEEE Veh. Technol. Mag.*, vol. 15, no. 1, pp. 16–26, Mar. 2020.
- [6] J. Karedal *et al.*, "A geometry-based stochastic MIMO model for vehicle-to-vehicle communications," *IEEE Trans. Wireless Commun.*, vol. 8, no. 7, pp. 3646–3657, Jul. 2009.
- [7] M. Yang *et al.*, "Non-stationary vehicular channel characterization in complicated scenarios," *IEEE Trans. Vehicular Technol.*, vol. 70, no. 9, pp. 8387–8400, Sep. 2021.
- [8] F. Liu *et al.*, "Joint radar and communication design: Applications, state-of-the-art, and the road ahead," *IEEE Trans. Commun.*, vol. 68, no. 6, pp. 3834–3862, Jun. 2020.
- [9] C. Huang *et al.*, "Geometry-cluster-based stochastic MIMO model for vehicle-to-vehicle communications in street canyon scenarios," *IEEE Trans. Wireless Commun.*, vol. 20, no. 2, pp. 755–770, Feb. 2021.
- [10] Z. Zhang *et al.*, "A general channel model for integrated sensing and communication scenarios," *IEEE Commun. Mag.*, vol. 61, no. 5, pp. 68–74, May 2023.
- [11] H. Jiang, B. Xiong, H. Zhang and E. Basar, "Hybrid far- and near-field modeling for reconfigurable intelligent surface assisted V2V channels: A sub-array partition based approach," *IEEE Trans. Wireless Commun.*, to be published. Doi: 10.1109/TWC.2023.3262063.
- [12] D. W. Matolak, I. Sen, and W. Xiong, "The 5-GHz airport surface area channel-Part I: Measurement and modeling results for large airports," *IEEE Trans. Vehicular Technol.*, vol. 57, no. 4, pp. 2014–2026, Jul. 2008.
- [13] Y. Yuan *et al.*, "3D wideband non-stationary geometry-based stochastic models for non-isotropic MIMO vehicle-to-vehicle channels," *IEEE Trans. Wireless Commun.*, vol. 14, no. 12, pp. 6883–6895, Dec. 2015.
- [14] Z. Huang and X. Cheng, "A 3D non-stationary model for beyond 5G and 6G vehicle-to-vehicle mmWave massive MIMO channels," *IEEE Trans. Intell. Transp. Syst.*, vol. 23, no. 7, pp. 8260–8276, Jul. 2022.
- [15] Z. Huang *et al.*, "A mixed-bouncing based non-stationarity and consistency 6G V2V channel model with continuously arbitrary trajectory," *IEEE Trans. Wireless Commun.*, to be published, 2023. Doi: 10.1109/TWC.2023.3293024.
- [16] *Technical Specification Group Radio Access Network; Study on Channel Model for Frequencies From 0.5 to 100 GHz (Release 14)*, document TR 38.901 Version 14.2.0, 3GPP, Sep. 2017. [Online]. Available: <http://www.3gpp.org/DynaReport/38901.htm>
- [17] Aalto University, AT&T, BUPT, CMCC, Ericsson, Huawei, Intel, KT Corporation, Nokia, NTT DOCOMO, New York University, Qualcomm, Samsung, University of Bristol, and University of Southern California. "5G channel model for bands up to 100 GHz." Oct. 2016. [Online]. Available: <http://www.5gworkshops.com/5GCM.html>
- [18] S. Manivasagam *et al.*, "LiDARsim: Realistic LiDAR simulation by leveraging the real world," in *Proc. IEEE/CVF Conf. Comput. Vis. Pattern Recognit. (CVPR)*, Seattle, WA, USA, Jun. 2020, pp. 11167–11176.
- [19] A. Geiger, P. Lenz, C. Stiller, and R. Urtasun, "Vision meets robotics: The KITTI dataset," *Int. J. Robot. Res.*, vol. 32, no. 11, pp. 1231–1237, Aug. 2013. Available: <https://www.DeepSense6G.net>
- [20] A. Klautau *et al.*, "5G MIMO data for machine learning: Application to beam-selection using deep learning," in *Proc. Inf. Theory Appl. Workshop (ITA)*, San Diego, CA, USA, Feb. 2018, pp. 1–9.
- [21] *Remcom. Wireless InSite.* [Online]. Available: <https://www.remcom.com/wireless-insite-em-propagation-software> [Publication date: Jan. 2017, Accessed date: Mar. 2022].
- [22] A. Klautau, N. González-Prelcic, and R. W. Heath, "LiDAR Data for Deep Learning-Based mmWave Beam-Selection," *IEEE Wireless Commun. Lett.*, vol. 8, no. 3, pp. 909–912, Jun. 2019.
- [23] M. Alrabeiah, A. Hredzak, Z. Liu, and A. Alkhatib, "ViWi: A deep learning dataset framework for vision-aided wireless communications," in *Proc. IEEE Veh. Technol. Conf. (VTC2020-Spring)*, Antwerp, Belgium, May 2020, pp. 1–5.
- [24] X. Cheng *et al.*, "M<sup>3</sup>SC: A generic dataset for mixed multi-modal (MMM) sensing and communication integration," *China Commun.*, to be published, 2023. [Online]. Available: <https://arxiv.org/abs/2306.14125>
- [25] S. Shah, D. Dey, C. Lovett, and A. Kapoor, "AirSim: High-fidelity visual and physical simulation for autonomous vehicles," in *Field and Service Robotics*, M. Hutter and R. Siegwart, Eds. Cham, Switzerland: Springer, 2018, pp. 621–635.
- [26] X. Cheng, Z. Huang, and S. Chen, "Vehicular communication channel measurement, modelling, and application for beyond 5G and 6G," *IET Commun.*, vol. 14, no. 19, pp. 3303–3311, Nov. 2020.
- [27] H. Jiang, B. Xiong, H. Zhang, and E. Basar, "Physics-based 3D end-to-end modeling for double-RIS assisted non-stationary UAV-to-ground communication channels," *IEEE Trans. Commun.*, vol. 71, no. 7, pp. 4247–4261, July 2023.
- [28] Z. Huang *et al.*, "A non-stationary 6G V2V channel model with continuously arbitrary trajectory," *IEEE Trans. Veh. Technol.*, vol. 72, no. 1, pp. 4–19, Jan. 2023.
- [29] Y. Chen, Y. Li, C. Han, Z. Yu, and G. Wang, "Channel measurement and ray-tracing-statistical hybrid modeling for low-terahertz indoor communications," *IEEE Trans. Wireless Commun.*, vol. 20, no. 12, pp. 8163–8176, Dec. 2021.
- [30] S. Wu, C.-X. Wang, H. Aggoune, M. M. Alwakeel, and X.-H. You, "A general 3-D non-stationary 5G wireless channel model," *IEEE Trans. Commun.*, vol. 66, no. 7, pp. 3065–3078, Jul. 2018.
- [31] J. Zhou *et al.*, "Channel modelling for vehicle-to-vehicle MIMO communications in geometrical rectangular tunnel scenarios," *IET Commun.*, vol. 14, no. 19, pp. 3420–3427, Oct. 2020.
- [32] M. Yang *et al.*, "A cluster-based three-dimensional channel model for vehicle-to-vehicle communications," *IEEE Trans. Vehicular Technol.*, vol. 68, no. 6, pp. 5208–5220, Jun. 2019.
- [33] P. Kyöstiet *et al.* (Sept. 2007). *WINNER II Channel Models, Version 1.1*. [Online]. Available: <http://www.ist-winner.org/WINNER2-Deliverables/D1.1.2v1.1.pdf>
- [34] C. A. Gutierrez, M. Patzold, W. Dahech, and N. Youssef, "A non-WSSUS mobile-to-mobile channel model assuming velocity variations of the mobile stations," in *Proc. IEEE WCNC'17*, San Francisco, CA, USA, Mar. 2017, pp. 1–6.
- [35] R. Verdone and A. Zanella, *Pervasive Mobile and Ambient Wireless Communications*. London: Springer, 2012.
- [36] A. O. Martinez, P. Eggers, and E. De Carvalho, "Geometry-based stochastic channel models for 5G: Extending key features for massive MIMO," in *Proc. IEEE 27th Annu. Int. Symp. Pers., Indoor, Mobile Radio Commun.*, Valencia, Spain, Sep. 2016, pp. 1–6.
- [37] A. F. Molisch, "A comprehensive model for ultrawideband propagation channels," in *Proc. IEEE GLOBECOM'05*, St. Louis, MO, USA, Dec. 2005, pp. 3648–3653.